

# Manufacturing an exact solution for 2D thermochemical mantle convection models

Sean James Trim<sup>1</sup>, Samuel L. Butler<sup>1</sup>, Shawn S.C. McAdam<sup>1</sup>, and Raymond J Spiteri<sup>1</sup>

<sup>1</sup>University of Saskatchewan

March 11, 2023

1                   **Manufacturing an exact solution for 2D**  
2                   **thermochemical mantle convection models**

3                   **S. J. Trim<sup>1</sup>, S. L. Butler<sup>2</sup>, S. S. C. McAdam<sup>1</sup>, and R. J. Spiteri<sup>1</sup>**

4                   <sup>1</sup>Department of Computer Science, University of Saskatchewan, Canada

5                   <sup>2</sup>Department of Geological Sciences, University of Saskatchewan, Canada

6                   **Key Points:**

- 7                   • An exact solution is manufactured for a realistic thermochemical mantle convec-
- 8                   tion flow in two dimensions.
- 9                   • An exact solution is highly useful for software verification and validation for prob-
- 10                  lems featuring sharply varying thermochemical flows.
- 11                  • Maple™ is used to assist with symbolic computations, and the resulting formulas
- 12                  are also provided in Fortran and Python.

**Abstract**

In this study, we manufacture an exact solution for a set of 2D thermochemical mantle convection problems. The derivation begins with the specification of a stream function corresponding to a non-stationary velocity field. The method of characteristics is then applied to determine an expression for composition consistent with the velocity field. The stream function formulation of the Stokes equation is then applied to solve for temperature. The derivation concludes with the application of the advection-diffusion equation for temperature to solve for the internal heating rate consistent with the velocity, composition, and temperature solutions. Due to the large number of terms, the internal heating rate is computed using Maple<sup>TM</sup>, and code is also made available in Fortran and Python. Using the method of characteristics allows the compositional transport equation to be solved without the addition of diffusion or source terms. As a result, compositional interfaces remain sharp throughout time and space in the exact solution. The exact solution presented allows for precision testing of thermochemical convection codes for correctness and accuracy.

**Plain Language Summary**

We manufacture an exact solution for a set of 2D thermochemical mantle convection problems, for which both thermal and compositional gradients impact buoyancy. Such problems must typically be solved approximately via computer models and are notoriously difficult to solve accurately. Our derivation uses a mathematical technique known as the method of characteristics that allows us to solve for composition and temperature variables without adding artificial terms to the model equations. Accordingly, our solution is able to feature sharp compositional gradients, which are difficult to model numerically. The exact solution facilitates the testing of thermochemical convection codes for both correctness and accuracy.

**1 Introduction****1.1 Motivation**

Buoyancy is the primary driving force behind convection in the Earth's mantle. Contributing factors to buoyancy in the mantle include lateral contrasts in temperature and composition. In the case of thermochemical flows, mantle buoyancy depends upon both of these factors. Heat sources and sinks affecting the thermal state of the Earth's mantle include radiogenic heating, heating from the outer core, and cooling at the Earth's surface (Turcotte & Schubert, 2002). Thermally driven buoyancy instabilities can arise when the rate of thermal transport via advection exceeds that of diffusion. Such situations include the rise of hot upwellings from the core and the descent of cold downwellings from the surface (e.g., a subducting slab). Buoyancy instabilities can also be caused by lateral variations in thermal boundary conditions. Lateral contrasts in mantle composition can occur for several reasons, including transitions between oceanic and continental lithosphere, rapid subduction of oceanic lithosphere, and deep dense compositional piles. The Earth's Large Low Shear wave Velocity Provinces (LLSVPs) may also be influenced by thermal and compositional gradients (Davies et al., 2015; McNamara, 2019).

Geophysical flows involving sharp compositional contrasts are notoriously difficult to model numerically. Challenges include both spurious oscillations and extraneous diffusion (Lenardic & Kaula, 1993). Numerical methods employed to minimize these errors include the use of particles (Tackley & King, 2003), level sets (Hillebrand et al., 2014), and hybrid methods (Samuel & Evonuk, 2010).

Another even more fundamental challenge is to ensure the software that implements the numerical solution has been coded correctly. By definition, model developers pro-

61 duce code to solve problems for which solutions are unknown. The verification and val-  
 62 idation process in modeling and simulation often involves qualitative comparison with  
 63 accepted published results or quantitative comparison with a highly accurate “reference  
 64 solution”. In the latter case, it can be questionable practice to use one’s own software  
 65 for verification purposes, or it potentially forces the developers to learn and use other  
 66 software. Accordingly, the presence of an exact solution with which numerical solutions  
 67 can be compared is highly desirable, especially if it is realistic. In this paper, we describe  
 68 a realistic 2D thermochemical mantle convection problem for which we manufacture an  
 69 exact solution.

## 70 1.2 Solution Features

71 Exact solutions applicable to mantle convection codes have been presented for sit-  
 72 uations including Stokes flow with lateral viscosity variations (Zhong, 1996; Duretz et  
 73 al., 2011; Pusok et al., 2017; Samuel, 2018), material deformation (Enright et al., 2002),  
 74 and compositional convection (Gassmüller et al., 2019). However, our manufactured so-  
 75 lution includes both thermal and compositional buoyancy effects, has a non-stationary  
 76 velocity field (Brunton & Rowley, 2010), and does not require the addition of source or  
 77 diffusion terms in the compositional transport equation. We believe that the inclusion  
 78 of these features brings the problem closer to practical thermochemical mantle convec-  
 79 tion models and allows for a greater range of numerical testing. For instance, having a  
 80 combination of thermal and compositional buoyancy effects allows testing the numer-  
 81 ical accuracy of the correlation between temperature and composition over a range of  
 82 buoyancy ratios. Further, a non-stationary velocity field allows for testing the efficacy  
 83 of numerical schemes for temporally variable velocity fields.

84 Additionally, deriving an exact solution without requiring compositional sources,  
 85 sinks, or diffusion ensures that compositional contrasts remain sharp, which is typically  
 86 the desired behavior in mantle convection studies. To accomplish this, we employ the  
 87 method of characteristics (Courant & Hilbert, 2008) for the analysis of compositional  
 88 transport. The method of characteristics has been previously applied to enhance the nu-  
 89 merical techniques for modeling compositional transport in geodynamic flows (De Smet  
 90 et al., 2000; Gerya & Yuen, 2003). In this study, we focus on applying the method of char-  
 91 acteristics to facilitate an exact solution to the compositional transport problem.

## 92 1.3 Derivation Outline

93 The primary steps of the derivation are as follows.

- 94 1. Prescribe a stream function that varies in time and space and corresponds to a  
 95 velocity field that is reasonable for mantle convection.
- 96 2. Apply the method of characteristics to find the time-dependent solution for the  
 97 composition field that matches the stream function.
- 98 3. Solve for the temperature given the stream function and the composition field by  
 99 applying the stream function formulation of the Stokes equation.
- 100 4. Determine the internal heating rate that corresponds to the stream function, tem-  
 101 perature, and composition fields using the advection-diffusion equation govern-  
 102 ing temperature.

103 The remainder of this paper provides details of the steps just described in the con-  
 104 text of a rectangular 2D domain with specific initial conditions, boundary conditions,  
 105 and stream function to yield a realistic velocity field. We note that the use of a prescribed  
 106 stream function to study compositional convection has been used previously (Kellogg &  
 107 Turcotte, 1990).

## 2 Method

### 2.1 Governing Equations

Although effectively solid over short time periods, the mantle acts as a highly viscous fluid over geologic time (Schubert et al., 2001). Mathematically, the mantle is typically modeled using a set of conservation equations obtained from fluid dynamics and thermodynamics. Specifically, the continuity equation specifies the conservation of mass, the Navier–Stokes equation models the conservation of momentum, and an advection–diffusion equation governs the conservation of energy. In addition, an advection equation is used to model compositional transport of distinct mantle components. We employ the Boussinesq approximation to simplify the effect of density variations. The infinite Prandtl number approximation is also used, for which the inertial terms in the Navier–Stokes equation are considered negligible (resulting in Stokes flow).

In the case of 2D incompressible flow in Cartesian coordinates, we may use the stream function formulation to simplify the treatment of the conservation of mass and momentum. Specifically, the non-dimensional biharmonic equation, given by

$$\frac{\partial^4 \psi}{\partial x^4} + \frac{\partial^4 \psi}{\partial x^2 \partial z^2} + \frac{\partial^4 \psi}{\partial z^4} = Ra_T \frac{\partial T}{\partial x} - Ra_C \frac{\partial C}{\partial x}, \quad (1)$$

may be used, where  $\psi$  is the stream function;  $T$  and  $C$  are the temperature and composition fields;  $x$  and  $z$  are the horizontal and vertical (increasing opposite to the direction of gravity) position coordinates; and  $Ra_T$  and  $Ra_C$  are the thermal and compositional Rayleigh numbers (Batchelor, 1967; van Keken et al., 1997). We note that equation 1 is the isoviscous form of the biharmonic equation. In principle, it is possible to include viscosity variations in the following derivation of a manufactured solution. However, this complicates the symbolic computations required to find formulas for the temperature and internal heating rate. Accordingly, we leave the inclusion of variable viscosity for a future study.

The velocity ( $\mathbf{v}$ ) is computed from the stream function using

$$\mathbf{v} = (u, w) = \left( \frac{\partial \psi}{\partial z}, -\frac{\partial \psi}{\partial x} \right), \quad (2)$$

where  $u$  and  $w$  are the horizontal and vertical velocity components, respectively. We note that equation 2 yields a velocity that is inherently divergence free. The stream function formulation reduces the number of scalar equations to be solved and removes the need to solve for the pressure, at the expense, however, of solving a higher-order equation.

The non-dimensional conservation equations for energy and composition are

$$\frac{\partial T}{\partial t} + \mathbf{v} \cdot \nabla T = \nabla^2 T + H, \quad (3)$$

and

$$\frac{\partial C}{\partial t} + \mathbf{v} \cdot \nabla C = 0, \quad (4)$$

respectively, where  $H$  is the internal heating rate and  $t$  is time.

The thermal Rayleigh number is

$$Ra_T = \frac{\alpha \rho_0 g \delta T D^3}{\kappa \eta_0}, \quad (5)$$

where  $\alpha$  is the thermal expansivity;  $\rho_0$  is surface density with  $C = T = 0$ ;  $g$  is the gravitational acceleration;  $\delta T$  is the temperature difference across the mantle;  $D$  is the mantle thickness;  $\kappa$  is thermal diffusivity; and  $\eta_0$  is the surface viscosity. The compositional Rayleigh number is

$$Ra_C = \frac{\delta \rho_C g D^3}{\kappa \eta_0}, \quad (6)$$

151 where  $\delta\rho_C$  is the compositional density contrast between enriched and ambient mantle  
152 materials.

## 153 2.2 Problem Setup

### 154 2.2.1 Problem Domain and Initial Conditions

155 We assume a problem domain  $[0, \lambda] \times [0, 1]$  in the  $x$ - $z$  plane, where  $\lambda > 0$  is the  
156 aspect ratio of the convecting cell.

157 We require initial conditions for both composition and temperature. For compo-  
158 sition, we select a two-layer initial state with a sharp contrast between layers that we  
159 denote by  $C(x, z, t = 0) = C_0(z)$ . In principle, this initial state may be achieved us-  
160 ing  $C_0(z) = \mathcal{H}(\frac{1}{2} - z)$ , where  $\mathcal{H}(\cdot)$  is the Heaviside function. However, we assume that  
161 the compositional interface be of non-zero thickness (see section 4.3), which is accom-  
162 plished using the logistic function as a smooth approximation to the Heaviside function

$$163 \quad C_0(z) = [1 + \exp[-2k(z_I - z)]]^{-1}, \quad (7)$$

164 where  $k$  controls the sharpness of the interface at  $z = z_I$ . For temperature, we have

$$165 \quad T(x, z, t = 0) = \frac{1}{Ra_T} \left[ -\frac{\pi^3(\lambda^2 + 1)^2}{\lambda^3} \cos(\pi x/\lambda) \sin(\pi z) f(t = 0) + Ra_C C_0(z) + (Ra_T - Ra_C)(1 - z) \right], \quad (8)$$

166 which is a hybrid between a conductive and layered profile (with layers corresponding  
167 to the initial composition field), with a sinusoidal perturbation. The perturbation is scaled  
168 by the initial value of the function  $f(t)$ , which controls the time dependence of the pre-  
169 sumed  $\psi$  (see section 3.1.1). This particular initial condition for  $T$  was chosen to sim-  
170 plify the treatment of internal heating in the derivation. However, other choices, such  
171 as a purely conductive profile, are possible with the appropriate choice of  $f_B(z, t)$  in equa-  
172 tion 43 below (see section 3.1 for details).

173 We note that the above initial conditions for  $C$  and  $T$  imply stable buoyancy for  
174  $t = 0$ . For our problem, convection is initiated by lateral gradients in the internal heat-  
175 ing rate (see section 3.1.5).

### 176 2.2.2 Boundary Conditions

177 To form a well-posed problem, boundary conditions are required for temperature  
178 and the velocity field. Our goal in selecting boundary conditions is to match realistic man-  
179 tle convection models as closely as possible. For temperature, we select insulating side-  
180 walls ( $\partial T/\partial x = 0$  at  $x = 0$  and  $x = \lambda$ ) and isothermal horizontal boundaries,  $T(x, z =$   
181  $0, t) = T_{bot}$  and  $T(x, z = 1, t) = T_{top}$ , where

$$182 \quad T_{bot} = \frac{Ra_C}{Ra_T} [C_0(0) - 1] + 1 \quad (9)$$

183 and

$$184 \quad T_{top} = \frac{Ra_C}{Ra_T} C_0(1). \quad (10)$$

185 The values of  $T_{bot}$  and  $T_{top}$  were selected to simplify the derivation of  $T$  and are consis-  
186 tent with the initial condition. Note that  $T_{bot}$  and  $T_{top}$  approach values of unity and zero,  
187 respectively, as the value of  $k$  increases. With these boundary conditions, the flow is char-  
188 acterized by mixed heating modes: basal and internal. For the velocity field, we choose  
189 impermeable ( $u = 0$  at  $x = 0$  and  $x = \lambda$ ,  $w = 0$  at  $z = 0$  and  $z = 1$ ) and free-slip  
190 ( $\partial u/\partial z = 0$  at  $z = 0$  and  $z = 1$ ,  $\partial w/\partial x = 0$  at  $x = 0$  and  $x = \lambda$ ) boundaries. Note  
191 that boundary fluxes of composition are zero due to the use of impermeable boundary  
192 conditions for velocity.

### 2.2.3 Diagnostics

The root-mean-square (RMS) velocity over the problem domain is defined as

$$v_{\text{RMS}} = \sqrt{\frac{1}{\lambda} \int_0^1 \int_0^\lambda [u^2 + w^2] dx dz} \quad (11)$$

and characterizes the overall vigor of convection. The entrainment is given by

$$E = \frac{1}{\lambda z_I} \int_{z_R}^1 \int_0^\lambda C dx dz, \quad (12)$$

which quantifies the proportion of material with  $C = 1$  above a reference height of  $z_R$ . In this study, we use  $z_R = z_I$ . These quantities have been used to help quantify the accuracy of numerical solutions in thermochemical convection studies (van Keken et al., 1997; Tackley & King, 2003; Samuel & Evonuk, 2010; S. J. Trim et al., 2020, 2021). We report the RMS velocity and entrainment for the manufactured solution in section 3.2.

## 3 Results

### 3.1 Derivation of the manufactured solution

We proceed with our derivation of the manufactured solution by finding the shape of the characteristic orbitals for a presumed stream function, followed by determining the time evolution along those orbitals. The method of characteristics can then be applied to find the solution for composition expressed as a transformation of its initial condition. The solution for temperature is then found from the biharmonic equation. Lastly, the internal heating rate for this problem is found from the advection-diffusion equation for temperature.

#### 3.1.1 Establishing the characteristic orbitals

Equation 4 can be expressed in 2D Cartesian coordinates as

$$\frac{\partial C}{\partial t} + u \frac{\partial C}{\partial x} + w \frac{\partial C}{\partial z} = 0. \quad (13)$$

We seek to describe the evolution of a characteristic curve with coordinates  $x(t)$  and  $z(t)$ . Along this characteristic, we have  $C = C(x(t), z(t), t)$  with time derivative given by

$$\frac{dC}{dt} = \frac{\partial C}{\partial x} \frac{dx}{dt} + \frac{\partial C}{\partial z} \frac{dz}{dt} + \frac{\partial C}{\partial t}. \quad (14)$$

Comparing equations 13–14, we extract a system of characteristic ODEs,

$$\begin{cases} dx/dt = u, \\ dz/dt = w, \\ dC/dt = 0. \end{cases} \quad (15)$$

Because  $dC/dt = 0$  along a characteristic, we have  $C(x(t), z(t), t) = C(x_0, z_0, 0)$ , where  $x_0 = x(0)$  and  $z_0 = z(0)$ . If we can solve for  $x_0$  and  $z_0$  in terms of  $x(t)$ ,  $z(t)$ , and  $t$ , we can obtain the exact time-dependent solution for  $C$ .

To obtain a suitable velocity field, we assume a stream function that satisfies the boundary conditions (see section 2.2.2) and is given by

$$\psi(x, z, t) = \sin(\pi x/\lambda) \sin(\pi z) f(t), \quad (16)$$

where  $f(t)$  is an integrable function of time. Using equation 2 in conjunction with equation 15, we obtain the characteristic ODEs governing the trajectories  $x(t)$  and  $z(t)$ , namely

$$\begin{cases} dx/dt = \pi \sin(\pi x/\lambda) \cos(\pi z) f(t), \\ dz/dt = -\frac{\pi}{\lambda} \cos(\pi x/\lambda) \sin(\pi z) f(t). \end{cases} \quad (17)$$

229 Dividing equations and rearranging gives

$$230 \quad \frac{1}{\lambda} \cot(\pi x/\lambda) dx = -\cot(\pi z) dz. \quad (18)$$

231 Integrating both sides of equation 18 gives

$$232 \quad \frac{1}{\lambda} \left[ \frac{\lambda}{\pi} \ln |\sin(\pi x/\lambda)| + D_1 \right] = - \left[ \frac{1}{\pi} \ln |\sin(\pi z)| + D_2 \right], \quad (19)$$

233 where  $D_1$  and  $D_2$  are constants of integration. Rearranging terms and applying the prop-  
234 erties of logarithms gives

$$235 \quad \ln |\sin(\pi x/\lambda) \sin(\pi z)| = -\pi(D_1/\lambda + D_2). \quad (20)$$

236 Exponentiating both sides results in

$$237 \quad |\sin(\pi x/\lambda) \sin(\pi z)| = D, \quad (21)$$

238 where  $D \equiv \exp[-\pi(D_1/\lambda + D_2)]$  is a constant. Sample contours of  $D$  for  $\lambda = 1$ , corre-  
239 sponding to characteristic orbital trajectories, are shown in figure 1. For the character-  
240 istics corresponding to a given value of  $D$ , equation 21 gives us the shape of the orbital  
241 path. However, we still need to determine the time dependence of the evolution of the  
242 characteristics to complete the solution.

### 243 **3.1.2 Time evolution of characteristics corresponding to $0 < D < 1$**

244 The initial condition for  $C$  consists of horizontal layers. Accordingly, equation 7  
245 is independent of  $x$ , and we need only analyze the time dependence of  $z$  as governed by  
246  $dz/dt$  in equation 17. Consequently, we must eliminate the  $\cos(\pi x/\lambda)$  term from  $dz/dt$   
247 in equation 17. The Pythagorean identity gives

$$248 \quad \cos(\pi x/\lambda) = S(x) \sqrt{1 - \sin^2(\pi x/\lambda)}, \quad (22)$$

249 where the function  $S(x)$  is defined by

$$250 \quad S(x) = \begin{cases} +1 & \text{if } x \leq \lambda/2, \\ -1 & \text{if } x > \lambda/2, \end{cases} \quad (23)$$

251 and is used to ensure the correct sign for the cosine function about  $x = \lambda/2$ . Using equa-  
252 tion 21 in equation 22, we obtain

$$253 \quad \cos(\pi x/\lambda) = S(x) \sqrt{1 - \frac{D^2}{\sin^2(\pi z)}}. \quad (24)$$

254 Substitution of equation 24 into equation 17 for  $dz/dt$  gives

$$\begin{aligned} \frac{dz}{dt} &= -\frac{\pi}{\lambda} f(t) S(x) \sqrt{\sin^2(\pi z) - D^2} \\ &= -\frac{\pi}{\lambda} f(t) S(x) (\pm iD) \sqrt{1 - \frac{1}{D^2} \sin^2(\pi z)} \\ &= \frac{i\pi D}{\lambda} f(t) S(x) \sqrt{1 - \frac{1}{D^2} \sin^2(\pi z)}, \end{aligned} \quad (25)$$

256 where we have retained the negative of the plus-minus sign to preserve the sign of the  
257 vertical velocity component. Rearranging equation 25 and multiplying both sides by  $\pi$   
258 gives

$$259 \quad \frac{d(\pi z)}{\sqrt{1 - \frac{1}{D^2} \sin^2(\pi z)}} = \frac{i\pi^2 D}{\lambda} f(t) S(x) dt. \quad (26)$$

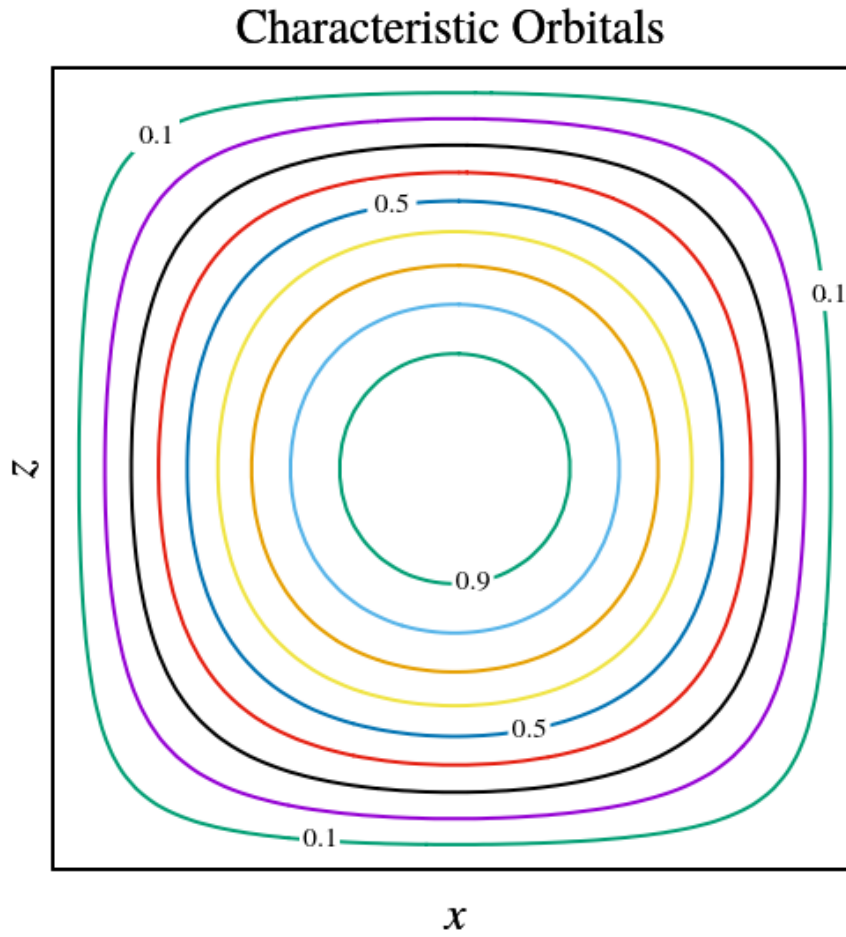


**Figure 1.** Sample contours of  $D$ , corresponding to characteristic orbitals, from equation 21 with  $\lambda = 1$ . Contour values range between 0.1–0.9 and are shown at intervals of 0.1. The value of  $D$  increases toward a value of unity at the center of the domain.

Integrating equation 26 along a particular characteristic, we obtain

$$\int_{\pi z_0}^{\pi z} \frac{d(\pi z)}{\sqrt{1 - \frac{1}{D^2} \sin^2(\pi z)}} = \frac{i\pi^2 D}{\lambda} \int_0^t f(t') S(x) dt', \quad (27)$$

where we have used  $t'$  to indicate the dummy variable of integration for time. We may evaluate the left side of equation 27 in terms of incomplete elliptic integrals of the first kind, giving

$$F\left(\pi z \left| \frac{1}{D^2} \right.\right) - F\left(\pi z_0 \left| \frac{1}{D^2} \right.\right) = \frac{i\pi^2 D}{\lambda} \int_0^t f(t') S(x) dt'. \quad (28)$$

We note that the left side only depends on the values of  $z_0$  and  $z$  along a characteristic orbital corresponding to the value of  $D$  (for  $0 < D < 1$ ). Importantly, the value of the left side does not depend on the path taken along the orbital between the vertical positions of  $z_0$  and  $z$ . Accordingly, we may simplify the integral on the right side by selecting paths  $x(t)$  along which the function  $S(x)$  does not change sign. However, for  $x \neq \lambda/2$ , each  $z$  value corresponds to two possible  $x$  values (one on either side of  $x = \lambda/2$ , as seen in figure 1). To account for all possible situations, we select two paths with  $x$  ranges given by: 1)  $x \leq \lambda/2$  and 2)  $x > \lambda/2$ . Path 1 starts with  $x_0 < \lambda/2$ , ends with  $x \leq \lambda/2$ , and has  $x(t) \leq \lambda/2$  for the entire range of integration:

$$F\left(\pi z \left| \frac{1}{D^2} \right.\right) - F\left(\pi z_0 \left| \frac{1}{D^2} \right.\right) = \frac{i\pi^2 D}{\lambda} \int_0^t f(t') dt'. \quad (29)$$

We note that this formula also applies for any case for which  $x \leq \lambda/2$ . Path 2 starts with  $x_0 > \lambda/2$ , ends with  $x > \lambda/2$ , and has  $x(t) > \lambda/2$  for the entire range of integration:

$$F\left(\pi z \left| \frac{1}{D^2} \right.\right) - F\left(\pi z_0 \left| \frac{1}{D^2} \right.\right) = \frac{i\pi^2 D}{\lambda} \int_0^t -f(t') dt'. \quad (30)$$

We note that this formula also applies for any case for which  $x > \lambda/2$ .

Isolating the  $z_0$  terms for all cases, we obtain

$$\begin{aligned} F\left(\pi z_0 \left| \frac{1}{D^2} \right.\right) &= \begin{cases} F\left(\pi z \left| \frac{1}{D^2} \right.\right) - \frac{i\pi^2 D}{\lambda} \int_0^t f(t') dt', & \text{if } x \leq \lambda/2, \\ F\left(\pi z \left| \frac{1}{D^2} \right.\right) + \frac{i\pi^2 D}{\lambda} \int_0^t f(t') dt', & \text{if } x > \lambda/2, \end{cases} \\ &= F\left(\pi z \left| \frac{1}{D^2} \right.\right) - S(x) \frac{i\pi^2 D}{\lambda} \int_0^t f(t') dt'. \end{aligned} \quad (31)$$

We may use the Jacobi elliptic function  $\text{cn}$  to extract the cosine of the elliptic amplitude, giving

$$\cos(\pi z_0) = \text{cn} \left\{ F\left(\pi z \left| \frac{1}{D^2} \right.\right) - S(x) \frac{i\pi^2 D}{\lambda} \int_0^t f(t') dt' \left| \frac{1}{D^2} \right. \right\}. \quad (32)$$

Finally, taking the inverse cosine gives

$$z_0 = \frac{1}{\pi} \arccos \left[ \text{cn} \left\{ F\left(\pi z \left| \frac{1}{D^2} \right.\right) - S(x) \frac{i\pi^2 D}{\lambda} \int_0^t f(t') dt' \left| \frac{1}{D^2} \right. \right\} \right]. \quad (33)$$

Equation 33 applies to all characteristics for  $0 < D < 1$ . This covers the majority of the domain, but it does not include the domain boundaries ( $D = 0$ ) nor the center of the domain ( $D = 1$ ). These two special cases for  $D$  are now addressed.

### 3.1.3 Time evolution of characteristics for $D = 0$ and $D = 1$

For  $D = 0$ , the characteristic orbital overlaps with the boundary of the domain. For the horizontal boundaries ( $z = 0, 1$ ), impermeability requires that  $z_0 = z$ . For the

294 vertical boundaries ( $x = 0, \lambda$ ), equation 25 gives

$$\begin{aligned}
 \frac{dz}{dt} &= -\frac{\pi}{\lambda} f(t) S(x) \sqrt{\sin^2(\pi z) - D^2} \\
 &= -\frac{\pi}{\lambda} f(t) S(x) |\sin(\pi z)|.
 \end{aligned}
 \tag{34}$$

296 Rearranging terms and integrating both sides gives

$$\int_{z_0}^z \csc(\pi z) dz = -\frac{\pi}{\lambda} \int_0^t f(t') S(x) dt'.
 \tag{35}$$

298 We are able to drop the absolute value sign for the left-hand integrand due to the range  
 299 of  $z$ . Also, the value of  $x$  along the vertical boundaries, denoted by  $x_b$ , is either 0 or  $\lambda$ .  
 300 Accordingly,  $x = x_b$  is constant in the right-hand integrand, and  $S(x_b)$  can be brought  
 301 outside of the integral. After integrating and isolating terms that depend on  $z_0$ , we obtain  
 302

$$\begin{aligned}
 \ln |\csc(\pi z_0) + \cot(\pi z_0)| &= \ln |\csc(\pi z) + \cot(\pi z)| - \frac{\pi}{\lambda} S(x_b) \int_0^t f(t') dt' \\
 &\equiv Q(z, t),
 \end{aligned}
 \tag{36}$$

304 where we use  $Q(z, t)$  to represent the right side of the equation to simplify the notation  
 305 that follows. To solve equation 36 for  $z_0 = z_0(z, t)$ , we make use of the substitution  $Z_0 =$   
 306  $\cot(\pi z_0)$ . For computational convenience, we presume a range of  $(-\pi/2, \pi/2] - \{0\}$  for  
 307 the corresponding inverse cotangent function, which will be used to recover  $z_0$ . Taking  
 308 the exponential of both sides of equation 36 and applying the  $Z_0$  substitution gives

$$\begin{aligned}
 e^Q &= |\csc(\pi z_0) + \cot(\pi z_0)| \\
 &= |\pm \sqrt{1 + Z_0^2} + Z_0|,
 \end{aligned}
 \tag{37}$$

310 where the plus-minus sign is positive for  $Z_0 \geq 0$  and negative for  $Z_0 < 0$ . Equation 37  
 311 has the admissible solution

$$Z_0 = -\frac{1}{2} [e^{-Q} - e^Q].
 \tag{38}$$

313 Accordingly, for  $D = 0$  at the sidewalls, we have

$$z_0 = \begin{cases} \frac{1}{\pi} \operatorname{arccot}(Z_0), & \text{if } Z_0 \geq 0, \\ 1 + \frac{1}{\pi} \operatorname{arccot}(Z_0), & \text{if } Z_0 < 0. \end{cases}
 \tag{39}$$

315 For  $D = 1$  in the problem domain, examination of equation 21 reveals that the  
 316 corresponding characteristic orbital consists of a single point at  $(x, z) = (\lambda/2, 1/2)$ . Sub-  
 317 stituting  $D = 1$  and  $z = 1/2$  into the right side of equation 25 results in  $dz/dt = 0$ ,  
 318 giving  $z_0 = z$ .

### 3.1.4 Solutions for $C$ and $T$

320 Combining the results from sections 3.1.2 and 3.1.3, we obtain

$$z_0 = \begin{cases} z, & \text{if } z = \{0, 1\} \text{ or } (x, z) = (\lambda/2, 1/2), \\ \frac{1}{\pi} \operatorname{arccot}(Z_0), & \text{if } x = \{0, \lambda\} \text{ and } Z_0 \geq 0, \\ 1 + \frac{1}{\pi} \operatorname{arccot}(Z_0), & \text{if } x = \{0, \lambda\} \text{ and } Z_0 < 0, \\ \frac{1}{\pi} \arccos \left[ \operatorname{cn} \left\{ F \left( \pi z \left| \frac{1}{D^2} \right. \right) - S(x) \frac{i\pi^2 D}{\lambda} \int_0^t f(t') dt' \left| \frac{1}{D^2} \right. \right\} \right], & \text{otherwise,} \end{cases}
 \tag{40}$$

321 which summarizes the evolution of characteristics for this problem. Equation 40 was de-  
 322 rived along characteristics for a given  $D$ . However, a more general form of the right side  
 323

324 may be achieved by applying the identity from equation 21. This substitution results in  
 325 a formula that applies to characteristics everywhere in the problem domain.

326 According to the method of characteristics, the time-dependent solution for  $C$  is  
 327 expressed as a transformation of its initial condition. Following this procedure results  
 328 in

$$329 \quad C(x, z, t) = C_0(z_0) = [1 + \exp[-2k(z_I - z_0)]]^{-1}, \quad (41)$$

330 where we may use equation 40 for the value of  $z_0$ .

331 Substituting equation 16 into equation 1 and integrating with respect to  $x$  gives

$$332 \quad Ra_T T - Ra_C C = -\frac{\pi^3(\lambda^2 + 1)^2}{\lambda^3} \cos(\pi x/\lambda) \sin(\pi z) f(t) + f_B(z, t), \quad (42)$$

333 where  $f_B(z, t)$  is an arbitrary function independent of  $x$ . Solving for  $T$  gives

$$334 \quad T(x, z, t) = \frac{1}{Ra_T} \left[ -\frac{\pi^3(\lambda^2 + 1)^2}{\lambda^3} \cos(\pi x/\lambda) \sin(\pi z) f(t) + f_B(z, t) + Ra_C C \right]. \quad (43)$$

335 We now aim to select  $f_B(z, t)$  to satisfy the isothermal boundary conditions for  $T$  at  $z =$   
 336  $0$  and  $z = 1$ . Due to impermeability at the boundaries, the initial condition results in  
 337  $C(x, z = 0, t) = C_0(0)$  and  $C(x, z = 1, t) = C_0(1)$ . Therefore, we may select  $f_B =$   
 338  $(Ra_T - Ra_C)(1 - z)$  to ensure that  $T(x, z = 0, t) = T_{bot}$  and  $T(x, z = 1, t) = T_{top}$  (see  
 339 section 2.2.2). This gives

$$340 \quad T(x, z, t) = \frac{1}{Ra_T} \left[ -\frac{\pi^3(\lambda^2 + 1)^2}{\lambda^3} \cos(\pi x/\lambda) \sin(\pi z) f(t) + Ra_C C + (Ra_T - Ra_C)(1 - z) \right]. \quad (44)$$

341 Furthermore, it can be verified that  $\partial T/\partial x = 0$  at  $x = 0$  and  $x = 1$ . This requires  
 342 showing that  $\partial C/\partial x = 0$  at  $x = 0$  and  $x = 1$  and may be done using the symmetry  
 343 of  $z_0$  about those boundaries. This symmetry can be established using equation 33 and  
 344 noting that  $D$  is symmetric about the sidewalls. Accordingly,  $T$  satisfies both isother-  
 345 mal conditions at the horizontal boundaries and insulating conditions at the vertical bound-  
 346 aries.

### 347 **3.1.5 Determining the expression for $H$**

348 Once the time-dependent solution with suitable boundary conditions is known, we  
 349 may use equation 3 to solve for  $H$  giving

$$350 \quad H(x, z, t) = \frac{\partial T}{\partial t} + \mathbf{v} \cdot \nabla T - \nabla^2 T. \quad (45)$$

351 Explicit evaluation of equation 45 is formidable due to a large number of terms. To this  
 352 end, a Maple™ (Maple 2022, 2022) script has been used to perform the symbolic com-  
 353 putations required. Routines that calculate  $H(x, z, t)$  based upon the formula derived  
 354 using Maple™ are available in Fortran and Python on GitHub and Zenodo (see section 6  
 355 for details).

## 356 **3.2 Benchmark Quantities**

357 Equation 11 can be used in conjunction with equation 2 to compute the RMS ve-  
 358 locity as

$$359 \quad v_{\text{RMS}}(t) = \frac{\pi\sqrt{\lambda^2 + 1}}{2\lambda} |f(t)|. \quad (46)$$

360 The  $v_{\text{RMS}}$  only depends on  $\lambda$  and  $f(t)$ , which are both known *a priori*. Accordingly,  $v_{\text{RMS}}$   
 361 does not explicitly depend on the evolution of  $C$ ,  $T$ , or  $H$ .

362 The entrainment, given by equation 12 with equation 41 as the integrand, is more  
 363 difficult to calculate. We were unable to find a closed-form solution. The next best al-  
 364 ternative is to perform numerical integration, which introduces a small amount of nu-  
 365 merical error due to spatial discretization. However, the result does not suffer from ac-  
 366 cumulation of error over time because temporal discretization is not required. In this pa-  
 367 per, we use the composite midpoint rule for the numerical integration of entrainment.  
 368 Both the RMS velocity and the entrainment may be used for benchmarking purposes.

### 369 3.3 Sample Results

#### 370 3.3.1 Temporally periodic flow

371 In this example, we present a flow that is periodic in time. Sample plots of tem-  
 372 perature, composition, and internal heating rate using  $f(t) = a \sin(\pi bt)$  with  $\lambda = 1$ ,  
 373  $a = 100$ ,  $b = 100$ ,  $z_I = 0.5$ ,  $k = 35$ , and  $Ra_T = 1 \times 10^5$  are shown in figure 2, where  
 374 the buoyancy ratio is given by  $B = Ra_C/Ra_T$ . At  $t = 0$ , there are no lateral varia-  
 375 tions in buoyancy, corresponding to a velocity field of zero throughout the domain. Lat-  
 376 eral gradients in thermal buoyancy are generated by the internal heating rate, which starts  
 377 the flow for  $t > 0$ . At  $t = 0.005$ , we have a hot upwelling of compositionally dense ma-  
 378 terial on the right and a cold downwelling of ambient material on the left, resulting from  
 379 counterclockwise flow. At  $t = 0.01$ , the counterclockwise flow has caused the compo-  
 380 sitionally dense material to descend through the left portion of the domain. Correspon-  
 381 dingly, the ambient material has ascended through the right portion of the domain, re-  
 382 sulting in a “jelly roll” pattern. The temperature fields for buoyancy ratios of 0.5 and  
 383 1 are similar in character overall. However, there is an additional thermal gradient in  
 384  $z$  throughout the domain for the  $B = 0.5$  case, due to the term  $(Ra_T - Ra_C)(1 - z)/Ra_T$   
 385 in equation 44. For  $B = 1$ , we have  $Ra_T = Ra_C$  which nullifies the contribution of  
 386 that term.

387 We also observe thin columns of hot compositionally dense and cold composition-  
 388 ally buoyant material for  $t > 0$  along the bottom right and top left sides, respectively.  
 389 These sharp gradients of  $C$  and  $T$  are due to impermeable boundary conditions and a  
 390 lack of diffusion. Impermeability results in boundary material being trapped along its  
 391 boundary. Also, the velocity of boundary material approaches zero as the domain cor-  
 392 ners are approached. This leads to the side wall material lagging behind nearby mate-  
 393 rial in the domain interior, generating sharp gradients. In addition to zero compositional  
 394 diffusivity,  $H$  exactly cancels thermal diffusion (see equation 45 and section 4.4). Accord-  
 395 ingly, the absence of diffusion preserves the sharp gradients in  $C$  and  $T$  near the side walls.  
 396

397 Snapshots of  $H$  corresponding to the cases shown in figure 2 are presented in fig-  
 398 ure 3. Due to the range of  $H$  values for these plots, a symmetric log scale was used for  
 399 the color scale for internal heating magnitudes greater than unity. For  $-1 < H < 1$ ,  
 400 a linear color mapping is used to avoid difficulties that a log scale would encounter near  
 401  $H = 0$ .

402 The internal heating rate impacts the thermal buoyancy so that the resulting ve-  
 403 locity field is consistent with the assumed stream function in equation 16. At  $t = 0$ ,  
 404  $H$  encourages counterclockwise flow in the upper and lower portions of the domain. How-  
 405 ever, counterclockwise flow is inhibited near the material interface, resulting in a low-  
 406 velocity counterclockwise flow to start. At  $t = 0.005$ ,  $H$  enhances counterclockwise flow  
 407 in most of the domain, resulting in vigorous flow. Finally, at  $t = 0.01$ ,  $H$  acts to gen-  
 408 erate clockwise flow because the choice of  $f(t)$  leads to a flow reversal at this time. For  
 409  $t = 0$  and  $0.01$ , the behavior of  $H$  is quite similar for  $B = 0.5$  and  $1$ . However, for  $t =$   
 410  $0.005$ , long wavelength  $H$  gradients independent of the compositional interface differ be-  
 411 tween  $B = 0.5$  and  $1$ .

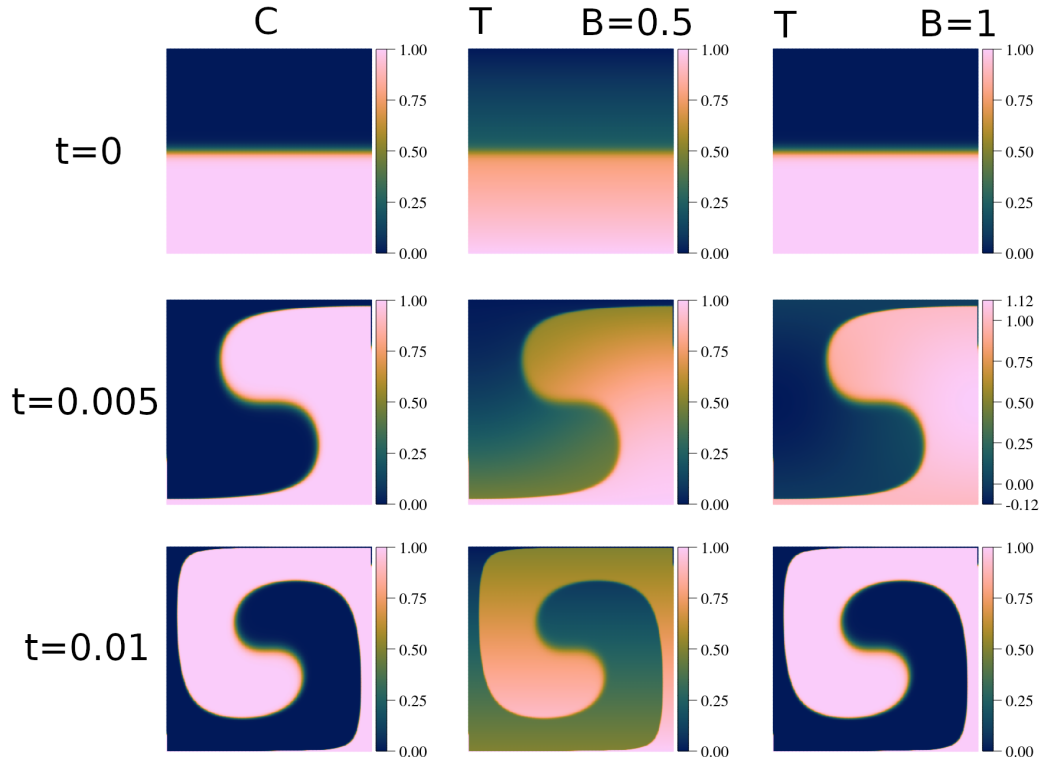


**Figure 2.** Plots of  $C$  and  $T$  using  $f(t) = a \sin(\pi bt)$  with  $\lambda = 1$ ,  $a = 100$ ,  $b = 100$ ,  $z_I = 0.5$ ,  $k = 35$ , and  $Ra_T = 1 \times 10^5$ . Temperature snapshots for buoyancy ratio values of 0.5 and 1.0 are shown. Time values are given in the leftmost portion of the figure.

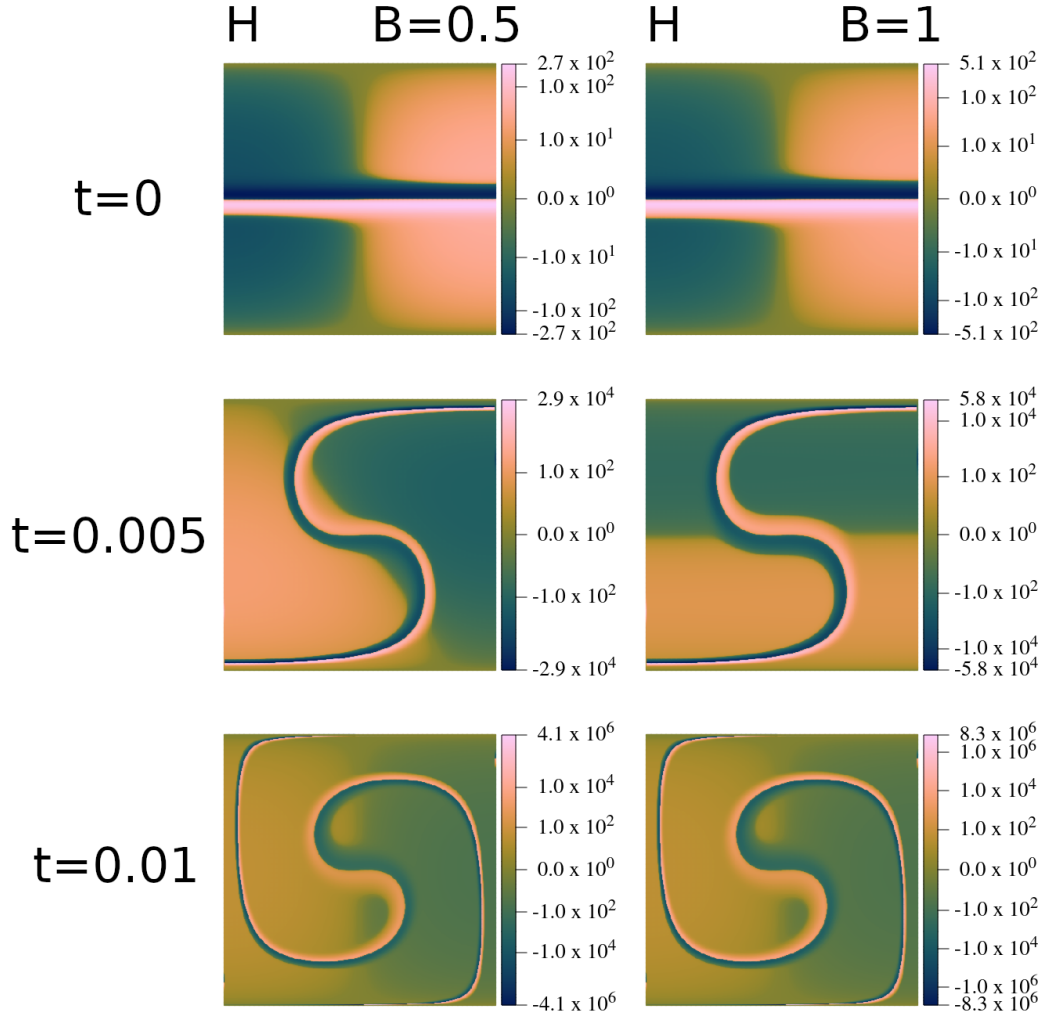


**Figure 3.** Plots of  $H$  using  $f(t) = a \sin(\pi bt)$  with  $\lambda = 1$ ,  $a = 100$ ,  $b = 100$ ,  $z_I = 0.5$ ,  $k = 35$ , and  $Ra_T = 1 \times 10^5$  are shown for buoyancy ratio values of 0.5 and 1.0. Time values are given in the leftmost portion of the figure. Note that a symmetric log scale is used for the color bar, except for  $-1 < H < 1$ , where a linear color mapping is used.

412 Plots of the velocity components and magnitude in terms of  $\lambda$  and  $f(t)$  are shown  
 413 in figure 4. For this sample problem, the leftmost column (i.e.,  $\lambda = 1$ ) applies, where  
 the extreme values of  $u$ ,  $w$ , and  $|\mathbf{v}|$  depend on the value of  $f(t)$ .

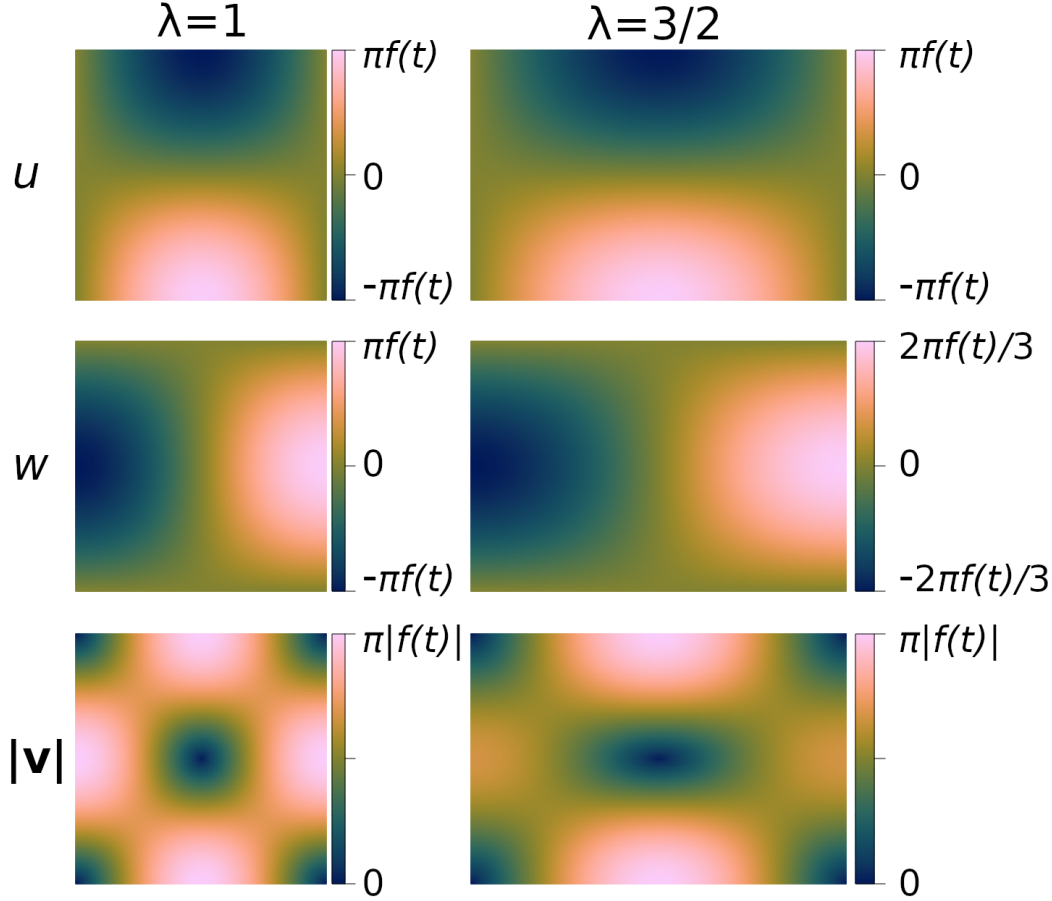


**Figure 4.** Plots of  $u$ ,  $w$ , and  $|\mathbf{v}|$  for  $\lambda = 1$  and  $\lambda = 3/2$ . Note that the color scale bounds depend on  $f(t)$ .

414

415 The exact RMS velocity and approximate entrainment values corresponding to the  
 416 selected parameters are shown in figure 5. Due to the choice of  $f(t)$ , the velocity field  
 417 is temporally periodic and has zero magnitude at times 0 and 0.01.

418 The initial entrainment is slightly above zero due to the reference  $z$  value ( $z_R =$   
 419  $z_I$ ) being situated in the center of the compositional interface. Accordingly, there is a  
 420 small amount of dense material that is already above  $z_R$  at  $t = 0$ . Subsequently, the  
 421 entrainment steadily rises to a peak value of approximately 0.7388 at  $t = 0.0062$ . Af-  
 422 terward, the head of the compositionally dense region begins to descend below  $z_R$ , lead-  
 423 ing to a decrease in entrainment. Finally, the entrainment value at  $t = 0.01$  is approx-  
 424 imately 0.5903.

425 We have selected the above parameters to be approximately consistent with a ther-  
 426 mochemical mantle convection model with a thermal Rayleigh number of  $10^5$ . For in-  
 427 stance, for the same domain and boundary conditions, the RMS velocity of purely ther-  
 428 mal convection at steady state has been observed to be under 200 units (see case 1b from

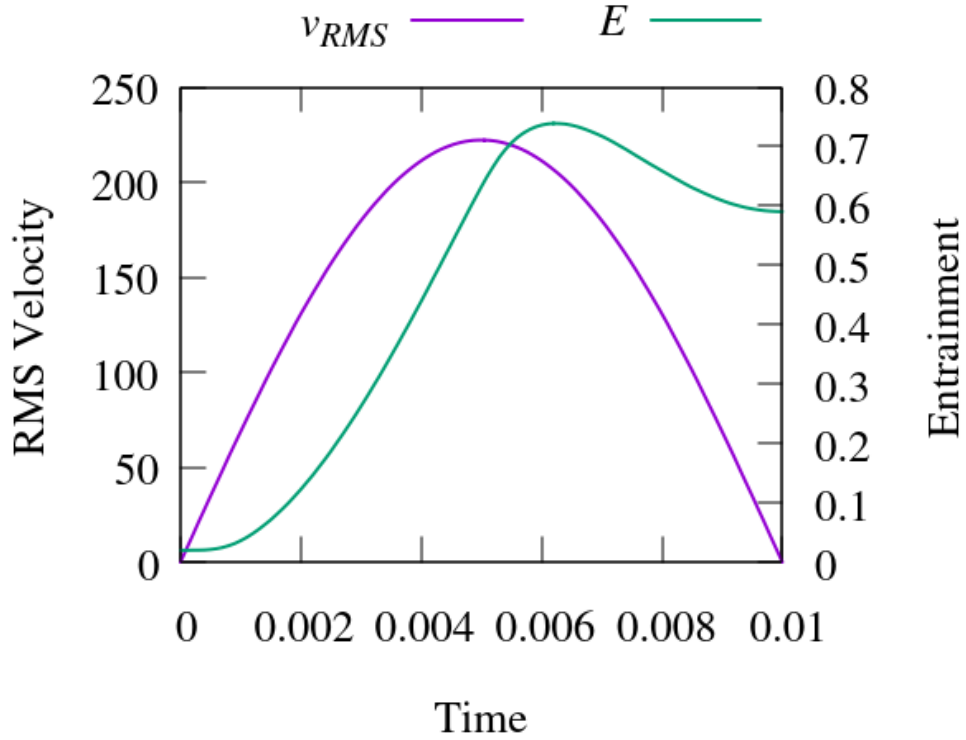


**Figure 5.** Plots of  $v_{RMS}$  and  $E$  using  $f(t) = a \sin(\pi bt)$  with  $\lambda = 1$ ,  $a = 100$ ,  $b = 100$ ,  $z_I = 0.5$ ,  $k = 35$ , and  $Ra_T = 1 \times 10^5$ . The entrainment was calculated using the composite midpoint rule with a uniformly spaced  $401 \times 401$  grid.

Blankenbach et al. (1989)). The mean RMS velocity for our sample parameters is  $100\sqrt{2} \approx 141.4$  units, which may be reasonable given that half the domain contains intrinsically dense material.

### 3.3.2 Approaching a steady state

In contrast to the example shown in section 3.3.1, we now present a case that approaches a steady state flow. Specifically, we use  $f(t) = a \sin(\pi bt)e^{-ct} + d$  with  $\lambda = 3/2$ ,  $a = 600/(\pi\sqrt{13})$ ,  $b = 100$ ,  $c = 50$ ,  $d = 4500/(\pi\sqrt{13})$ ,  $z_I = 0.2$ ,  $k = 35$ ,  $Ra_T = 1 \times 10^6$ , and  $Ra_C = 8 \times 10^5$ . Figure 6 shows snapshots of  $C$  and  $T$  for several time values between 0 and 0.1. At  $t = 0$ , the solution begins with a basal layer of hot compositionally dense material that is 0.2 units thick. Subsequently, the basal layer begins to undergo shearing in a counterclockwise direction. Early evolution of  $C$  for  $t = 0$  to  $t = 0.005$  is shown in figure 7, where we observe the transformation of the initial dense layer into a spiraling band due to rotational shear. Unlike section 3.3.1, the flow continues in a counterclockwise direction as time elapses. By  $t = 0.025$  (figure 6), the dense material has been sheared into a spiral pattern. The number of spiral turns is proportional to the number of mantle overturns. This quantity can be estimated by integrating the RMS velocity with respect to time, which estimates the number of transits across the depth of the mantle, and dividing by four. For  $t = 0.025$ , we have approximately five overturns. By  $t = 0.05$ , nearly ten overturns have occurred, corresponding to an increase in spiral turns. Continued shearing results in thinning of the spiral layer. By  $t = 0.075$ , we have approximately 14 overturns, with a further decrease in spiral layer thickness. Finally, by  $t = 0.1$ , approximately 19 overturns have occurred and the flow is near a steady state. The spiral layer has become even thinner due to shearing.

It is interesting to note that compositionally dense material is localized to the outer perimeter of the domain, even as  $t$  approaches infinity. Specifically, the dense material cannot pass the characteristic orbital given by the largest value of  $D$  within the basal layer at  $t = 0$ ; the orbital barrier is given by  $D = \sin(\pi z_I) \approx 0.588$  (see figure 1 for reference). Strictly speaking, this  $D$  value holds for  $C > 0.5$  because we used the center of the initial compositional interface in our calculation. The orbital barrier for the remaining dense material corresponds to a slightly larger  $D$ , due to the thickness of the compositional interface at  $t = 0$ .

Snapshots of  $H$  for the same times in figure 6 are shown in figure 8. Here  $H$  can be described as a superposition of features corresponding to 1) the compositional layer and 2) a long wavelength gradient stemming from terms independent of  $C$  in equation 44. For all times shown, the long wavelength component introduces asymmetry that promotes counterclockwise flow. For  $t = 0$ , we observe that compositionally dense material is heated internally between  $x = 0$  and  $x \approx 2\lambda/3$ , while material just above the interface is cooled internally. At  $t = 0.025$ , we observe that the dense material spiral is heated near the compositional interface, while the less compositionally dense material just beyond the interface is cooled. This trend holds for  $t \geq 0.025$  but becomes less pronounced as time increases. We also note that the innermost spirals in  $H$  are located closer to the domain center than those of  $C$  or  $T$  (see figure 6). The  $H$  spirals corresponding to  $D > 0.588$  only impact material with  $C < 0.5$  (with the majority near or at  $C = 0$ ). For  $t \in [0.05, 0.1]$ , the spiral band becomes thinner as time elapses, similar to  $C$  and  $T$ . In addition, it is observed that the innermost position of the spiral band does not change significantly.

As before, figure 4 shows the velocity components and magnitude in terms of  $\lambda$  and  $f(t)$ . For this problem, the rightmost column in the figure (i.e.,  $\lambda = 3/2$ ) applies, where extreme values of  $u$ ,  $w$ , and  $|\mathbf{v}|$  depend on the value of  $f(t)$ .

Figure 9 shows the exact RMS velocity and the approximate entrainment versus time for this sample problem. The RMS velocity gradually approaches a steady-state value of 750 units. As time increases, the RMS velocity oscillates with decreasing amplitude

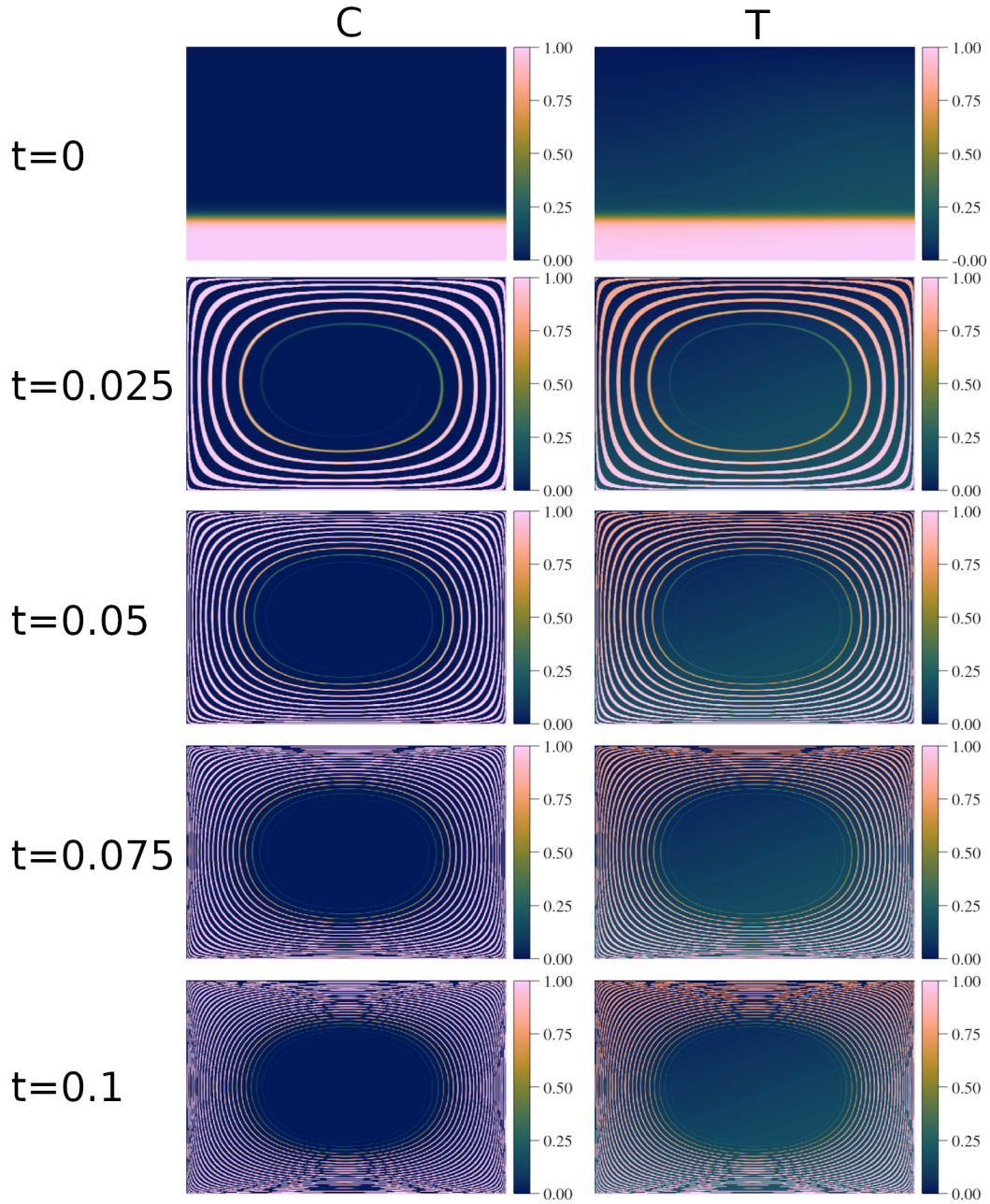


**Figure 6.** Plots of  $C$  and  $T$  using  $f(t) = a \sin(\pi bt)e^{-ct} + d$  with  $\lambda = 3/2$ ,  $a = 600/(\pi\sqrt{13})$ ,  $b = 100$ ,  $c = 50$ ,  $d = 4500/(\pi\sqrt{13})$ ,  $z_I = 0.2$ ,  $k = 35$ ,  $Ra_T = 1 \times 10^6$ , and  $Ra_C = 8 \times 10^5$ . Time values are given in the leftmost portion of the figure.

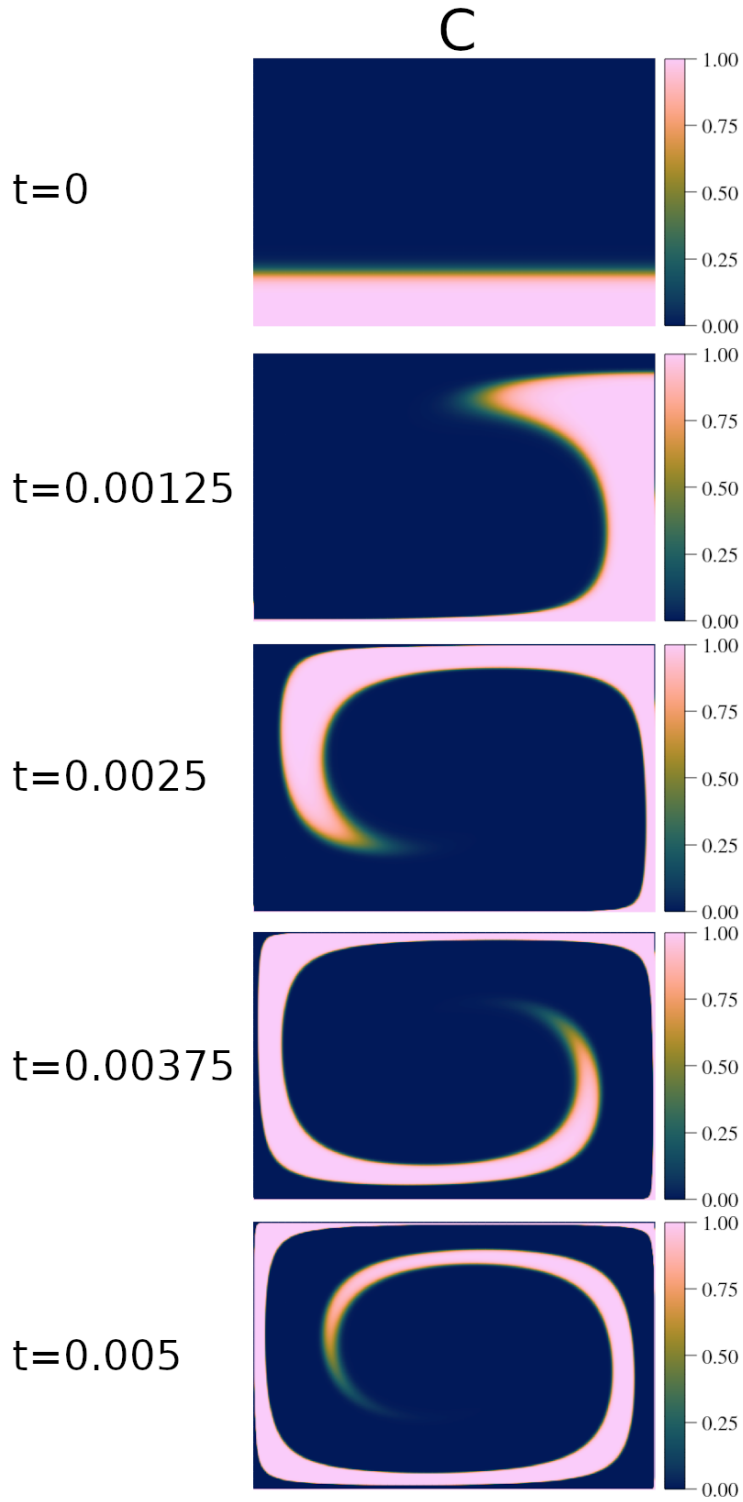


**Figure 7.** Plots of  $C$  at early stages of evolution using  $f(t) = a \sin(\pi bt)e^{-ct} + d$  with  $\lambda = 3/2$ ,  $a = 600/(\pi\sqrt{13})$ ,  $b = 100$ ,  $c = 50$ ,  $d = 4500/(\pi\sqrt{13})$ ,  $z_I = 0.2$ ,  $k = 35$ ,  $Ra_T = 1 \times 10^6$ , and  $Ra_C = 8 \times 10^5$ . Time values are given in the leftmost portion of the figure.

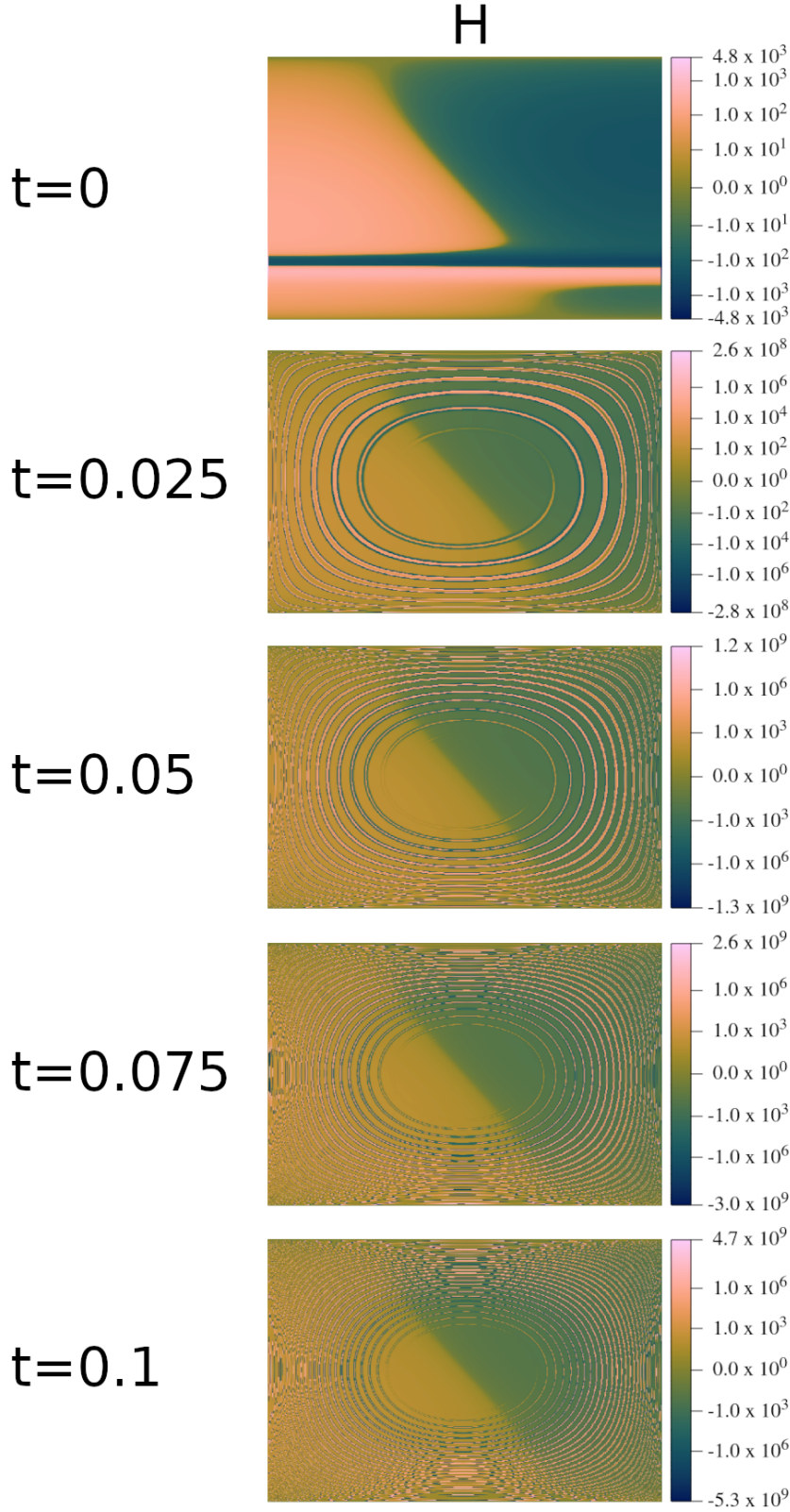


**Figure 8.** Plots of  $H$  using  $f(t) = a \sin(\pi b t) e^{-ct} + d$  with  $\lambda = 3/2$ ,  $a = 600/(\pi\sqrt{13})$ ,  $b = 100$ ,  $c = 50$ ,  $d = 4500/(\pi\sqrt{13})$ ,  $z_I = 0.2$ ,  $k = 35$ ,  $Ra_T = 1 \times 10^6$ , and  $Ra_C = 8 \times 10^5$ . Time values are given in the leftmost portion of the figure. A symmetric log scale is used for the color bar, except for  $-1 < H < 1$ , where a linear color mapping is used.

480 about the steady-state value. The steady-state RMS velocity value was selected (via  $d$ )  
 481 to be a bit less than that observed in previous benchmarks for thermal mantle convec-  
 482 tion (see problem 1c from Blankenbach et al. (1989)). It was presumed that the pres-  
 483 ence of dense material consisting of 20% of the domain volume would result in a decreased  
 RMS velocity.

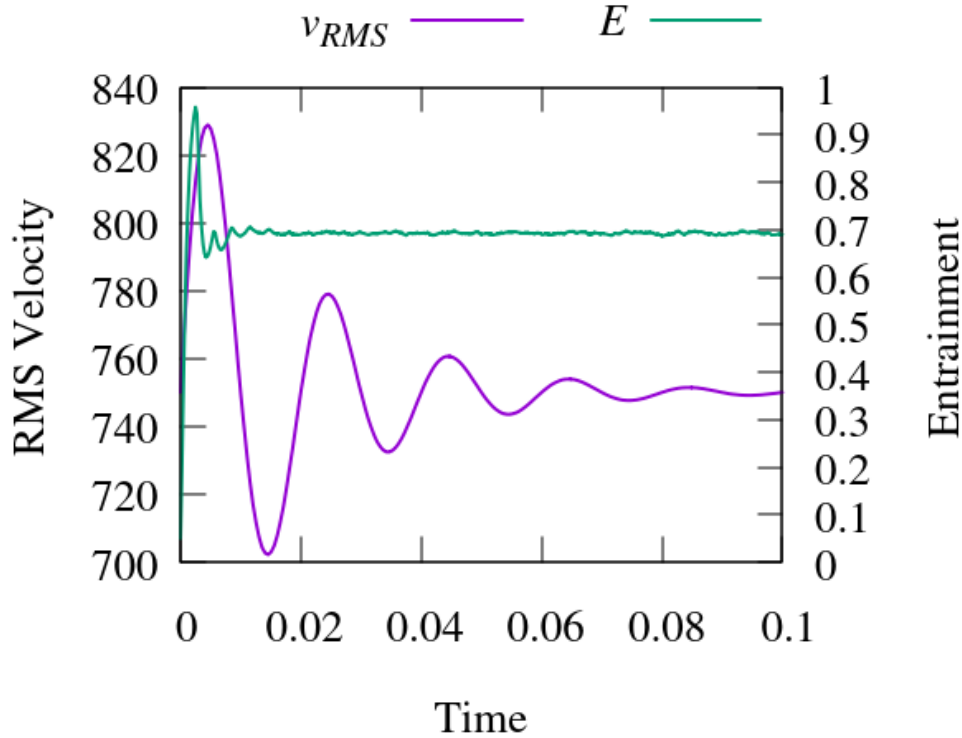


**Figure 9.** Plots of  $v_{RMS}$  and  $E$  using  $f(t) = a \sin(\pi bt)e^{-ct} + d$  with  $\lambda = 3/2$ ,  $a = 600/(\pi\sqrt{13})$ ,  $b = 100$ ,  $c = 50$ ,  $d = 4500/(\pi\sqrt{13})$ ,  $z_I = 0.2$ ,  $k = 35$ ,  $Ra_T = 1 \times 10^6$ , and  $Ra_C = 8 \times 10^5$ . The entrainment was calculated using the composite midpoint rule with a uniformly spaced  $751 \times 501$  grid.

484

485 As in section 3.3.1, the initial entrainment is slightly above zero due to  $z_R$  being  
 486 situated in the center of the compositional interface. The entrainment sharply increases  
 487 until reaching a peak value of approximately 0.9575 at  $t = 0.0025$  ( $C$  shown in figure 7).  
 488 Following that, the entrainment quickly reaches a quasi steady state beyond about  $t =$   
 489  $0.02$  with an average entrainment value of 0.6923. During that period, the amount of dense  
 490 material that is transported above  $z_R$  nearly matches the amount of dense material that  
 491 descends below  $z_R$ .

## 482 4 Discussion

### 483 4.1 Use in mantle convection codes

484 In this study, we have manufactured an exact solution for a problem that can be  
 485 set up in many mantle convection codes. We now discuss the necessary steps for code  
 486 setup to generate numerical solutions for comparison with the manufactured solution pre-  
 487 sented in this paper. The setup steps are as follows:

488

- 498 1. Select values for physical constants  $\lambda$ ,  $z_I$ ,  $k$ ,  $Ra_T$ , and  $Ra_C$ .
- 499 2. Select a function  $f(t)$  and values for any associated parameters (e.g.,  $a$  and  $b$  for  
500  $f(t) = a \sin(\pi bt)$ ).
- 501 3. Set initial conditions according to section 2.2.1.
- 502 4. Set boundary conditions according to section 2.2.2.
- 503 5. Set the internal heating rate according to the routines provided via GitHub/Zenodo  
504 (see section 6 for details).

505 After these setup steps are complete, the model can be run forward in time with the set-  
506 tings that require testing (e.g., resolution, particle count, time integration scheme, etc.).  
507 We note that time accuracy can be precisely quantified using the derived solutions; the  
508 inability to precisely quantify time accuracy has been a challenge for thermochemical con-  
509 vection codes (van Keken et al., 1997).

510 Steps 1–3 are straightforward. For particle methods, step 4 may pose a challenge  
511 in terms of setting up the initial condition for  $C$  due to the requirement of a specific thick-  
512 ness and gradient in the compositional interface. If particles track both compositions (e.g.,  
513 the ratio method outlined in Tackley and King (2003)) and can support intermediate  $C$   
514 values between 0 and 1, the interface can be precisely set using equation 7. However, if  
515 only one composition is tracked (e.g., the absolute method described in van Keken et al.  
516 (1997) and Tackley and King (2003)) or particles do not support intermediate  $C$  values,  
517 equation 7 is more difficult to satisfy for the interface. One possibility is to select  $k$  so  
518 that the initial interface thickness matches that which is available in the code. However,  
519 this does not guarantee that the gradient of  $C$  will match that of equation 7. This lim-  
520 itation may lead to discrepancies between the numerical and manufactured solutions. In  
521 addition, initializing particles along the domain boundaries may help to resolve the sharp  
522 gradients observed there.

523 Step 5 may also require some extra programming if internal heating rates that vary  
524 in space and time are not available in the code of interest. For a successful test, the vari-  
525 able internal heating rate must be updated sufficiently often in the code (e.g., once per  
526 stage of a Runge–Kutta time integration scheme).

527 To calculate  $H$  correctly, numerical implementations of elliptic integrals of the first  
528 and second kinds are required and must allow a Jacobi amplitude range of at least  $[0, \pi]$ .  
529 Additionally, implementations of the Jacobi elliptic functions (sn, cn, dn) must permit  
530 complex first arguments. Both the elliptic integral and Jacobi elliptic functions must al-  
531 low elliptic parameter values greater than unity. We note that this functionality is not  
532 standard in all software packages. However, the Fortran (and Python) routines provided  
533 in section 6 satisfy these requirements by applying generalizations to the algorithms pre-  
534 sented in Fukushima (2012, 2013).

535 Due to a large number of terms and relatively expensive function evaluations for  
536  $F$  and cn, the calculation of  $H$  may be non-trivial. Because  $H$  takes the form of a source  
537 term in equation 3 and is time varying, it needs to be evaluated each time the numer-  
538 ical method makes a right-hand side function evaluation. This may adversely impact the  
539 computation time required to generate numerical approximations to the exact solution.

540 We note that  $T$  values can be negative or exceed unity in the solution. Accordingly,  
541 numerical schemes must allow such values for  $T$ . Also, codes must allow top and bot-  
542 tom boundary temperatures other than zero and unity for best results (see section 2.2.2).

## 543 4.2 Testing with a Convection Code

544 In this section, we test the functionality of the software used to compute  $H$  with  
545 the convection code ProjecTracer (S. J. Trim et al., 2020). The code features a particle-  
546 in-cell method for the advection of both temperature and composition, while velocity (via

a stream function formulation) and thermal diffusion are computed on an Eulerian mesh using centered finite differences. Our calculations were produced using a uniform Eulerian mesh consisting of  $n \times n$  ( $n$  ranges between 200 and 800) cells with fourth-order finite differences. Each Eulerian dual grid cell was initialized with 60 tracer particles and bilinear shape functions were used to interpolate particle values to the Eulerian grid. Time integration was performed using the explicit two-stage, second-order midpoint Runge–Kutta method with a Courant factor of 0.99. We consider the temporally periodic problem from section 3.3.1 with  $B = 0.5$ .

Figure 10 shows a comparison between numerical and exact solutions for  $C$ ,  $T$ , and  $\psi$  at  $t = 0.0025$  for  $n = 800$ . We observe that the numerical results generally match the exact solution. However, the numerical solution did not capture the sharp gradients near the domain boundaries for  $C$  and  $T$  in the exact solution. This may be due to an overestimation of thermal diffusion at the boundaries in the numerical solution. Placing tracer particles specifically on the domain boundaries improved accuracy in the numerical results. However, it is expected that mesh refinement near the boundaries would improve accuracy further. Also, the magnitude of  $\psi$  is underestimated in the numerical solution, likely due to the accumulation of error over time.

Figure 11 shows time series of  $v_{\text{RMS}}$ , the logarithm of the  $v_{\text{RMS}}$  error magnitude, and the entrainment for different values of  $n$ . We observe that the numerical solutions approach the exact (or semi-exact in the case of entrainment as in section 3.2) solution as  $n$  increases. For the time interval considered, errors may be within an acceptable tolerance, particularly for large  $n$ . However, error is observed to accumulate over time. Accordingly, for longer integration times it may be a challenge to maintain an acceptable error tolerance. This is a common occurrence in practice due to a combination of many factors including sensitivity of the equations, the numerical method employed, and floating-point arithmetic. In such situations, increasing the spatial resolution or decreasing the time step size may lead to improved results.

### 4.3 Thickness of the compositional interface

The interface thickness between distinct compositions must be non-zero for the internal heating rate to remain bounded. For example, if the Heaviside function is used to specify the initial condition for  $C$ , then  $H$  contains terms including the Dirac delta function and its derivatives. This poses a challenge for convection codes because it is not practical to implement an internal heating rate that is not bounded. For these reasons, we have selected a smooth approximation to the Heaviside function for the initial condition for  $C$ . However, with a sufficiently large  $k$  value, the interface thickness can in principle be made as sharp as needed.

### 4.4 The sharpness of temperature contrasts

In situations where the stream function (or velocity field) is smooth, gradients in temperature are of similar sharpness to those of composition. This similarity can be seen by examining equation 1. This is also the case for our manufactured solution and can be seen in figure 2.

Additionally, from equation 45 it is observed that  $H$  is partially comprised of a negative diffusion term. Accordingly,  $H$  contributes to the sharpness of temperature gradients in the exact solution.

Therefore, the numerical method used for the advection-diffusion equation for temperature should be capable of handling sharp gradients. One possibility is to apply particle methods for temperature in a similar fashion to their use for composition (Gerya & Yuen, 2003; S. J. Trim et al., 2020).

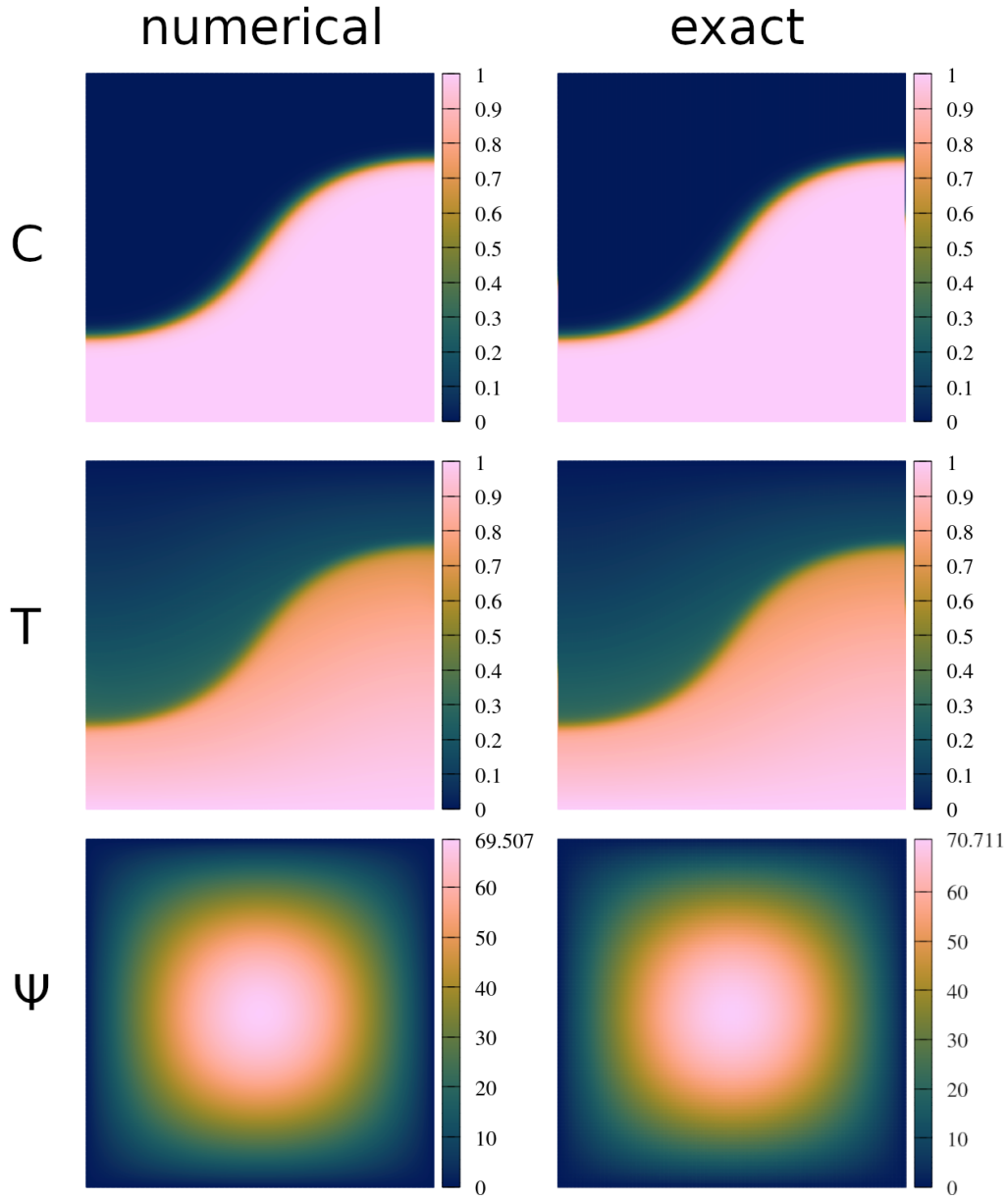


**Figure 10.** Snapshots of  $C$ ,  $T$ , and  $\psi$  at  $t = 0.0025$  using  $f(t) = a \sin(\pi bt)$  with  $\lambda = 1$ ,  $a = 100$ ,  $b = 100$ ,  $z_I = 0.5$ ,  $k = 35$ ,  $Ra_T = 1 \times 10^5$ , and  $Ra_C = 0.5 \times 10^5$ . Numerical results computed using ProjecTracer are shown in the left column, and exact solutions are shown in the right column.

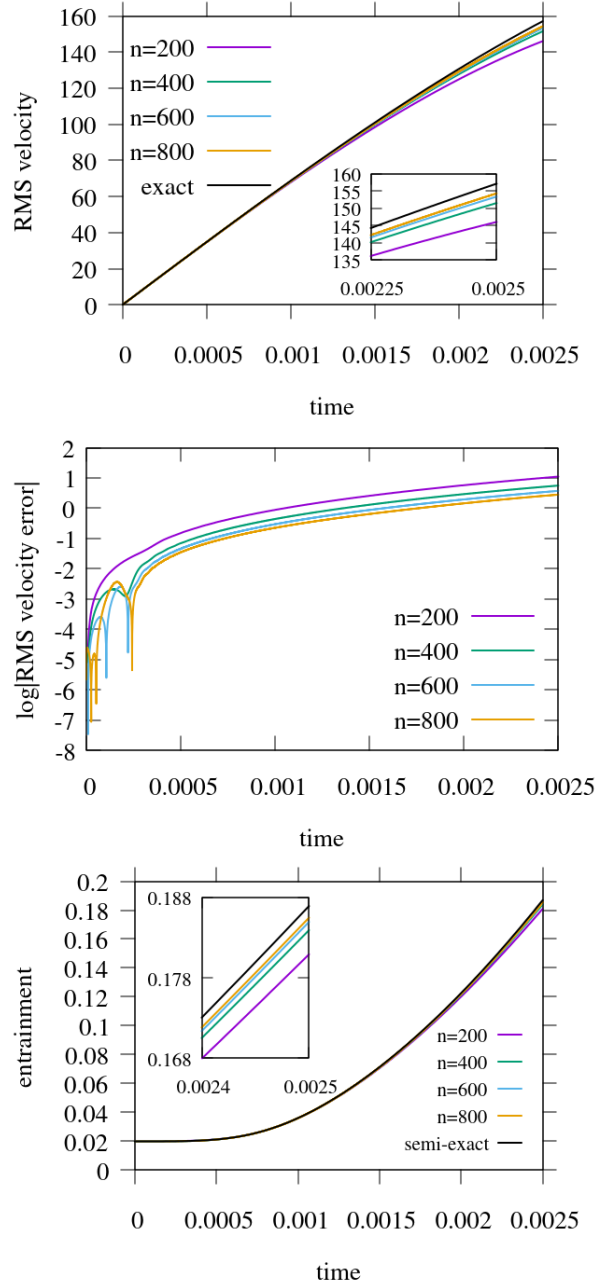


**Figure 11.** Time series of  $v_{RMS}$ , the logarithm of the  $v_{RMS}$  error magnitude, and the entrainment using  $f(t) = a \sin(\pi bt)$  with  $\lambda = 1$ ,  $a = 100$ ,  $b = 100$ ,  $z_I = 0.5$ ,  $k = 35$ ,  $Ra_T = 1 \times 10^5$ , and  $Ra_C = 0.5 \times 10^5$ . Results were obtained using ProjecTracer with a  $n \times n$  Eulerian mesh, where  $n$  is given in the plot legends. Inset plots are shown for a more precise view of final evolution. For  $v_{RMS}$ , the exact solution is shown for reference. For entrainment, a semi-exact curve is shown for reference, calculated by applying the composite midpoint rule with a uniform  $800 \times 800$  mesh according to section 3.2.

## 4.5 Extension to 3D

Extension of the derivation to 3D would also provide a useful test of code accuracy and correctness beyond 2D flows. However, several complexities would need to be addressed for a 3D manufactured solution, including an increased number of variables and equations. For instance, using poloidal-toroidal decomposition, we can describe the flow velocity with two scalar potentials. In that case, the 3D Stokes equation can be reduced to two scalar equations (Chandrasekhar, 2013). The determination of suitable characteristic orbitals would also be more challenging and may involve multiple parameters (as opposed to just  $D$  in the 2D case). Nonetheless, a 3D solution would be helpful for testing community codes and is worthy of future exploration.

## 5 Conclusions

Using the method of characteristics, a manufactured solution is derived for isoviscous 2D thermochemical mantle convection models for a prescribed stream function. Exact expressions for velocity, temperature, composition, and internal heating rate are derived. Due to the large number of terms, the expression for the internal heating rate is found using computer algebra software and is provided on GitHub and Zenodo in Maple™, Fortran, and Python (see section 6). The solution features a non-stationary velocity field, thermal and compositional buoyancy effects, and a sharp compositional interface. The method of characteristics facilitates a solution without additional diffusion or source terms in the compositional transport equation, allowing the preservation of sharp compositional interfaces in time and space. For the problem posed, the sharpness of temperature contrasts is similar to that of composition. The exact solution can be used to test the correctness and accuracy of thermochemical mantle convection codes and allows precise evaluation of the accuracy of numerical solutions for all problem variables in time and space.

## 6 Open Research

Software-related files and data supporting this article are maintained on GitHub (<https://github.com/seantrim/exact-thermochem-solution>) and archived on Zenodo (S. Trim, 2023a). Files include a computer algebra script for Maple™ (Maple 2022, 2022) that was used for the symbolic computation of  $H$ . In addition, Fortran files containing the formula for  $H$ , translated from Maple™ results, and related functions/routines are provided. Scripts for Python compatibility are also available.

Calculations in section 4.2 were performed using ProjecTracer, available on GitHub (<https://github.com/seantrim/ProjecTracer>) and Zenodo (S. Trim, 2023b).

Figures in this article were made using SageMath (SageMath, 2022), Gnuplot (Williams et al., 2021), GIMP (GIMP: GNU Image Manipulation Program, 2021), and MATLAB® (MATLAB, 2022). SageMath (<https://www.sagemath.org>), Gnuplot (<http://www.gnuplot.info>), and GIMP (<https://www.gimp.org>) are available via free licenses. Plots of  $C$ ,  $T$ , and  $H$  were made using the perceptually uniform batlow color map (Cramer et al., 2020) and is available on Zenodo (Cramer, 2021). Maple™ (<https://www.maplesoft.com>) and MATLAB® (<https://www.mathworks.com>) have commercial licenses but are often available through institutional access. Maple™ is a trademark of Waterloo Maple Inc.

## Acknowledgments

We would like to thank Henri Samuel and Cedric Thieulot for thoughtful reviews. S.J.T, S.S.C.M, and R.J.S are grateful for funding from the Natural Sciences and Engineering Research Council of Canada under its Discovery Grant Program (RGPN-2020-04467 (R.J.S)) and Undergraduate Student Research Award Program (S.S.C.M.). S.L.B is also grate-

642 ful for funding from the Natural Sciences and Engineering Research Council of Canada  
643 (RGPN-2020-06332).

## 644 References

- 645 Batchelor, G. (1967). An introduction to fluid dynamics. 1967. *Cambridge,,: UP*  
646 *xviii, 615*.
- 647 Blankenbach, B., Busse, F., Christensen, U., Cserepes, L., Gunkel, D., Hansen, U.,  
648 ... others (1989). A benchmark comparison for mantle convection codes.  
649 *Geophysical Journal International*, 98(1), 23–38.
- 650 Brunton, S. L., & Rowley, C. W. (2010). Fast computation of finite-time lyapunov  
651 exponent fields for unsteady flows. *Chaos: An Interdisciplinary Journal of*  
652 *Nonlinear Science*, 20(1), 017503.
- 653 Chandrasekhar, S. (2013). *Hydrodynamic and hydromagnetic stability*. Courier Cor-  
654 poration.
- 655 Courant, R., & Hilbert, D. (2008). *Methods of mathematical physics: partial differ-*  
656 *ential equations*. John Wiley & Sons.
- 657 Cramer, F. (2021, September). *Scientific colour maps*. Zenodo. Retrieved from  
658 <https://doi.org/10.5281/zenodo.5501399> (The development of the Sci-  
659 entific colour maps is not funded any longer, but will continue as a pro bono  
660 project for the scientific community. - Fabio) doi: 10.5281/zenodo.5501399
- 661 Cramer, F., Shephard, G. E., & Heron, P. J. (2020). The misuse of colour in science  
662 communication. *Nature communications*, 11(1), 5444.
- 663 Davies, D., Goes, S., & Lau, H. (2015). Thermally dominated deep mantle llsvps: a  
664 review. *The Earth's heterogeneous mantle*, 441–477.
- 665 De Smet, J. H., Van Den Berg, A. P., Vlaar, N. J., & Yuen, D. A. (2000). A  
666 characteristics-based method for solving the transport equation and its ap-  
667 plication to the process of mantle differentiation and continental root growth.  
668 *Geophysical Journal International*, 140(3), 651–659.
- 669 Duretz, T., May, D. A., Gerya, T., & Tackley, P. (2011). Discretization errors and  
670 free surface stabilization in the finite difference and marker-in-cell method for  
671 applied geodynamics: A numerical study. *Geochemistry, Geophysics, Geosys-*  
672 *tems*, 12(7).
- 673 Enright, D., Fedkiw, R., Ferziger, J., & Mitchell, I. (2002). A hybrid particle  
674 level set method for improved interface capturing. *Journal of Computational*  
675 *physics*, 183(1), 83–116.
- 676 Fukushima, T. (2012). Precise and fast computation of a general incomplete elliptic  
677 integral of third kind by half and double argument transformations. *Journal of*  
678 *Computational and Applied Mathematics*, 236(7), 1961–1975.
- 679 Fukushima, T. (2013). Precise and fast computation of jacobian elliptic functions by  
680 conditional duplication. *Numerische Mathematik*, 123(4), 585–605.
- 681 Gassmüller, R., Lokavarapu, H., Bangerth, W., & Puckett, E. G. (2019). Evaluating  
682 the accuracy of hybrid finite element/particle-in-cell methods for modelling  
683 incompressible stokes flow. *Geophysical Journal International*, 219(3), 1915–  
684 1938.
- 685 Gerya, T. V., & Yuen, D. A. (2003). Characteristics-based marker-in-cell method  
686 with conservative finite-differences schemes for modeling geological flows with  
687 strongly variable transport properties. *Physics of the Earth and Planetary*  
688 *Interiors*, 140(4), 293–318.
- 689 GIMP: GNU Image Manipulation Program. (2021). *version 2.10.30*. [https://www](https://www.gimp.org)  
690 [.gimp.org](https://www.gimp.org).
- 691 Hillebrand, B., Thieulot, C., Geenen, T., Van Den Berg, A., & Spakman, W. (2014).  
692 Using the level set method in geodynamical modeling of multi-material flows  
693 and earth's free surface. *Solid Earth*, 5(2), 1087–1098.

- 694 Kellogg, L., & Turcotte, D. (1990). Mixing and the distribution of heterogeneities in  
695 a chaotically convecting mantle. *Journal of Geophysical Research: Solid Earth*,  
696 *95*(B1), 421–432.
- 697 Lenardic, A., & Kaula, W. (1993). A numerical treatment of geodynamic viscous  
698 flow problems involving the advection of material interfaces. *Journal of Geo-*  
699 *physical Research: Solid Earth*, *98*(B5), 8243–8260.
- 700 Maple 2022. (2022). *Maplesoft, a division of waterloo maple inc.* Waterloo Maple  
701 Inc. <https://www.maplesoft.com>.
- 702 MATLAB. (2022). *version 9.12.0 (r2022a)*. The MathWorks Inc. [https://www](https://www.mathworks.com)  
703 [.mathworks.com](https://www.mathworks.com).
- 704 McNamara, A. K. (2019). A review of large low shear velocity provinces and ultra  
705 low velocity zones. *Tectonophysics*, *760*, 199–220.
- 706 Pusok, A. E., Kaus, B. J., & Popov, A. A. (2017). On the quality of velocity inter-  
707 polation schemes for marker-in-cell method and staggered grids. *Pure and Ap-*  
708 *plied Geophysics*, *174*, 1071–1089.
- 709 Samuel, H. (2018). A deformable particle-in-cell method for advective transport in  
710 geodynamic modelling. *Geophysical Journal International*, *214*(3), 1744–1773.
- 711 Samuel, H., & Evonuk, M. (2010). Modeling advection in geophysical flows with par-  
712 ticle level sets. *Geochemistry, Geophysics, Geosystems*, *11*(8).
- 713 Schubert, G., Turcotte, D. L., & Olson, P. (2001). *Mantle convection in the earth*  
714 *and planets*. Cambridge University Press.
- 715 Tackley, P. J., & King, S. D. (2003). Testing the tracer ratio method for modeling  
716 active compositional fields in mantle convection simulations. *Geochem. Geo-*  
717 *phys. Geosys.*, *4*(4).
- 718 The Sage Developers. (2022). Sagemath, the Sage Mathematics Software System  
719 (Version 9.5) [Computer software manual]. (<https://www.sagemath.org>)
- 720 Trim, S. (2023a, February). *seantrim/exact-thermochem-solution: Release 1.2.0*.  
721 Zenodo. Retrieved from <https://doi.org/10.5281/zenodo.7671498> doi: 10  
722 [.5281/zenodo.7671498](https://doi.org/10.5281/zenodo.7671498)
- 723 Trim, S. (2023b, February). *seantrim/projecttracer: Release 1.2.0*. Zen-  
724 odo. Retrieved from <https://doi.org/10.5281/zenodo.7671666> doi:  
725 [10.5281/zenodo.7671666](https://doi.org/10.5281/zenodo.7671666)
- 726 Trim, S. J., Butler, S. L., & Spiteri, R. J. (2021). Benchmarking multiphysics soft-  
727 ware for mantle convection. *Computers & Geosciences*, *154*, 104797.
- 728 Trim, S. J., Lowman, J. P., & Butler, S. L. (2020). Improving mass conservation  
729 with the tracer ratio method: application to thermochemical mantle flows.  
730 *Geochemistry, Geophysics, Geosystems*, *21*(2), e2019GC008799.
- 731 Turcotte, D. L., & Schubert, G. (2002). *Geodynamics*. Cambridge university press.
- 732 van Keken, P., King, S., Schmeling, H., Christensen, U., Neumeister, D., & Doin,  
733 M.-P. (1997). A comparison of methods for the modeling of thermochemical  
734 convection. *Journal of Geophysical Research: Solid Earth*, *102*(B10), 22477–  
735 22495.
- 736 Williams, T., Kelley, C., & many others. (2021, June). *Gnuplot 5.4: an interactive*  
737 *plotting program*. <http://www.gnuplot.info/>.
- 738 Zhong, S. (1996). Analytic solutions for stokes’ flow with lateral variations in viscos-  
739 ity. *Geophysical Journal International*, *124*(1), 18–28.